The International Journal of Advanced Manufacturing Technology (2022) 121:4099–4113
https://doi.org/10.1007/s00170-022-09606-1

ORIGINAL ARTICLE

Nanosecond laser polishing of laser nitrided Zr-based metallic glass surface

Hu Huang[1] · Jing Hong[1] · Yongfeng Qian[1] · Chao Wang[1] · Zhiyu Zhang[2] · Lin Zhang[3]

Received: 8 February 2022 / Accepted: 23 June 2022 / Published online: 2 July 2022

Abstract

Nanosecond pulsed laser nitriding is a promising technique for improving the surface hardness of Zr-based metallic glass (MG). However, being different from conventional surface enhancement methods, this method generally results in irregular surface profile and poor surface roughness, which impedes its potential industrial applications and popularization. Here, nanosecond laser polishing (LP), as a novel post-machining flattening approach, is introduced to flatten the laser nitrided Zr-based MG surface. The effects of the LP parameters, i.e., laser power, scanning speed, and track overlap, on the micro-topography and surface roughness (*Sa* and *Sq*) of the laser nitrided MG surface are systematically investigated, as well as the surface hardness variation. Compared with the laser nitrided Zr-based MG surface, homogeneous surface morphologies are achieved by LP with a remarkable reduction on surface roughness (*Sa*) by 93.7%, 72.9%, and 84.6% on three demonstrated laser nitrided MG surfaces. Most of the defects occurred in laser nitriding are removed under the optimal LP conditions. According to the residual micro-morphology on the LP surface, two kinds of mechanisms in LP are discussed. This study demonstrates that LP is an important alternative to effectively improve the surface roughness and mechanical performance of laser nitrided Zr-based MG, which would be meaningful and significant for the functional applications of MG in bio-chemical and anti-corrosion interface.

Keywords Pulsed laser polishing · Nanosecond laser · Laser nitriding · Metallic glass · Surface roughness

Abbreviations

LP	Laser polishing
FLP	First laser polishing
SLP	Second laser polishing
P	Laser power
V	Scanning speed
f	Pulse frequency
r	Laser spot radius
dx	Pulse distance
dy	Track pitch
O	Pulse overlap
R	Track overlap
E	Energy density

1 Introduction

Metallic glasses (MGs) were first investigated in the preparation of Au–Si amorphous alloys in the 1960s [1]. After that, more achievements were made in the 1980s and a variety of MGs with high glass-forming ability were developed [2–4]. Compared with their crystalline counterparts, MGs present some outstanding properties, such as superior strength, high elasticity, and excellent corrosion resistance [5–7]. These attractive properties act as a trigger for numerous potential applications for MGs in aerospace, precision machinery, military weapons, and consumer electronic fields [8, 9]. However, MGs suffer from highly localized shear banding deformation at

✉ Hu Huang
huanghu@jlu.edu.cn

✉ Lin Zhang
zhanglin@keio.jp

[1] Key Laboratory of CNC Equipment Reliability, Ministry of Education, School of Mechanical and Aerospace Engineering, Electron Microscopy Center, Jilin University, Changchun, Jilin 130022, China

[2] Key Laboratory of Optical System Advanced Manufacturing Technology, Changchun Institute of Optics, Fine Mechanics and Physics, Chinese Academy of Sciences, Changchun, China

[3] Department of Mechanical Engineering, Faculty of Science and Technology, Keio University, Yokohama 223-8522, Japan

ambient temperature, limiting their extensive applications as structural and engineering materials [10, 11]. Nevertheless, the high hardness and anti-corrosion properties of MGs compared to many crystalline alloys extend some novel and creative applications as surface functional materials. Thus, it is essential to focus on their surface physical and chemical properties to satisfy application demands.

Laser processing [12–18] as an effective approach has been intensively investigated to modify the surface micromorphology and corresponding properties. According to different processing conditions, the irradiated surfaces can be tailored from softening, such as laser shock peening, to hardening, such as laser-induced nitriding, by adjusting structure or doping components. For example, laser shock peening was utilized to soften the MG surface by introducing free volume [14, 18]. On the other hand, after laser irradiation in nitrogen atmosphere, a thin layer of ZrN was generated on the irradiated surface as a result of laser-induced nitriding, resulting in the surface hardening [19]. In general, severe material ablation simultaneously occurs during the laser nitriding of Zr-based MG surface, leading to irregular surface morphologies and poor surface roughness. Lot of surface defects are left with the laser nitriding, such as humps, dents, and micro-sized particles, which hinder its further applications as functional surfaces.

To solve this problem, LP as a novel approach is introduced to flatten the laser nitrided Zr-based MG surface. This approach avoids the environmental pollution that commonly occurs in electrochemical polishing [20], as well as the uncontrollable removal rate of surface layer in mechanical abrasive polishing [21]. What's more, LP makes it possible to spend less machining time, focus on selected localized area, and produce no waste and effluents [22–25]. In particular, LP could be performed on the same position without resetting after laser nitriding, which avoids further post-machining treatments and the corresponding positioning deviations in the following machining.

This study attempted to verify the feasibility of LP for flattening laser nitrided Zr-based MG surface, and three types of laser nitrided surfaces with different initial morphologies as demonstrations were produced first. The effects of the LP parameters, i.e., laser power, scanning speed, and track overlap, on surface roughness (*S*a and *S*q) of laser nitrided Zr-based MG surfaces were systematically investigated, and the corresponding mechanisms with different laser powers and scanning speeds were discussed. The surface microstructure and surface hardness before and after LP were also measured. Finally, the optimal LP conditions for flattening the laser nitrided Zr-based MG surface were obtained, which should be able to provide some valuable reference for the LP experiments on other similar kinds of materials.

2 Materials and experiments

2.1 Materials

The metallic glass ($Zr_{41.2}Ti_{13.8}Cu_{12.5}Ni_{10}Be_{22.5}$) with the dimensional size of 20 mm × 20 mm × 2 mm was bought from Peshing New Metal Material (Changzhou) Co., Ltd., China. It was prepared by arc melting the constituting elements of Zr, Ti, Cu, Ni, and Be (purity high than 99.9 wt%) in a Tigettered argon atmosphere via the copper mold suck-casting method. The ingot was re-melted several times and stirred with a magnetic beater to obtain the MG sample with compositional homogeneity. In order to remove the crystallized layer that may be generated during the manufacturing process and obtain a smooth surface, the sample was mechanically polished with 400, 800, 1200, and 2000 grit sand papers in subsequence by a precision lapping/polishing machine (UNIPOL-802, MTI corporation, China), and finalized with polishing pad and diamond abrasive paste. The polished sample was cleaned up by acetone and alcohol to remove the chips and abrasives on the final polished surface.

2.2 Preparation of laser nitrided surfaces

A fiber nanosecond pulsed laser system (SP-050P-A-EP-Z-F-Y, SPI Lasers, UK), characterized by a wavelength of 1064 nm, pulse width of 10 ns, and pulse frequency of 600 kHz, was employed to irradiate the MG samples in nitrogen atmosphere for preparing the laser nitrided surfaces. The laser irradiation system together with scanning strategy is illustrated in Fig. 1. The laser beam is focused on the MG surface by a F-theta lens and moves along the scanning direction. After single-line irradiation, the laser beam is offset by a distance relative to the previous scanning track, and line irradiation is performed again. The parameters involved in the scanning strategy can be described by the following equations [26–29]:

$$d_x = V/f \tag{1}$$

$$O = 1 - d_x/(2r) \tag{2}$$

$$R = 1 - d_y/(2r) \tag{3}$$

where V is the scanning speed, f stands for the pulse frequency, r represents the laser spot radius, dx is the pulse distance between two adjacent laser spots, dy is the track pitch between two adjacent scanning tracks, and O and R represent the pulse overlap and track overlap. According to the previous research [19] and pre-experiments, the detailed parameters for laser nitriding are listed in Table 1. A slow scanning speed of 1 mm/s was selected for promoting the

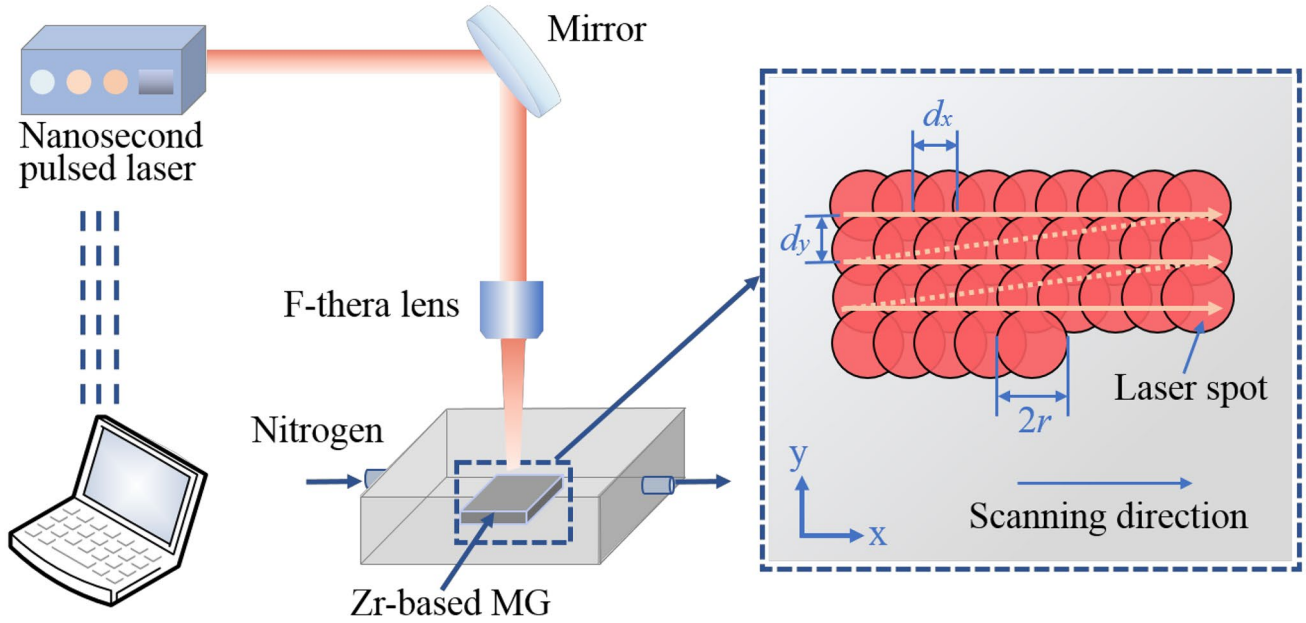

Fig. 1 The schematic diagram of the laser irradiation system and scanning strategy

laser nitriding. To explore the capability of LP, laser powers, 0.95, 1.56, and 2.78 W, were selected to obtain three types of nitrided surfaces with different surface morphologies and surface roughness, which are defined as surfaces A, B, and C. To ensure the comparability of experimental results, surfaces A, B, and C were located on the same surface of one single sample.

2.3 LP process

After laser nitriding, the same nanosecond pulsed laser system was employed to flatten the laser nitrided surfaces A, B, and C. In order to protect the sample surface from oxidization in LP, the sample was also placed in the chamber under nitrogen atmosphere during the further LP process. As reported in Ref. [30], during the process of LP, the irradiated region generally undergoes complex physical changes, such as the re-melting and solidification of surface materials. According to the degree of melting, two typical melt-related LP mechanisms are found, i.e., surface shallow melting (SSM) and surface over melting (SOM) [30–32], as shown in Fig. 2a, b respectively. For the SSM mechanism, only partial peaks are melted under relatively low laser energy, and the materials of melted peak fill up the valleys due to capillary pressure and gravity [32], leading to the improvement on surface flatness and roughness. In terms of the SOM mechanism, a high laser energy causes the thickness of the melted layer larger than the height difference between peaks and valleys, and a molten pool is formed. The surface materials in the irradiated region are redistributed due to capillary pressure and thermal capillary pressure [31]. However, since the materials in the irradiated region are over-melted, convective currents in molten pool generally cause capillary waves, and thus the surface flatness is commonly worse than that under SSM.

Table 1 Laser nitriding parameters corresponding to surfaces A, B, and C

	Laser power (W)	Scanning speed (mm/s)	Track overlap (%)
Surface A	2.78	1	50
Surface B	1.56	1	50
Surface C	0.95	1	50

2.3.1 LP process for surface A

Since the laser power used for surface A was the highest, remarkable material ablation occurred, generating lots of micro-grooves and particles on the laser nitrided surface. Considering the large roughness of surface A, further subsequent LP process was divided into two stages, i.e., the first laser polishing (FLP) and second laser polishing (SLP). FLP was used to greatly reduce the surface roughness, and then SLP was further employed to remove the residual defects on the surface after FLP. The schematic diagram of LP on surface A is presented in Fig. 3. A series of LP parameters, laser power (P), scanning speed

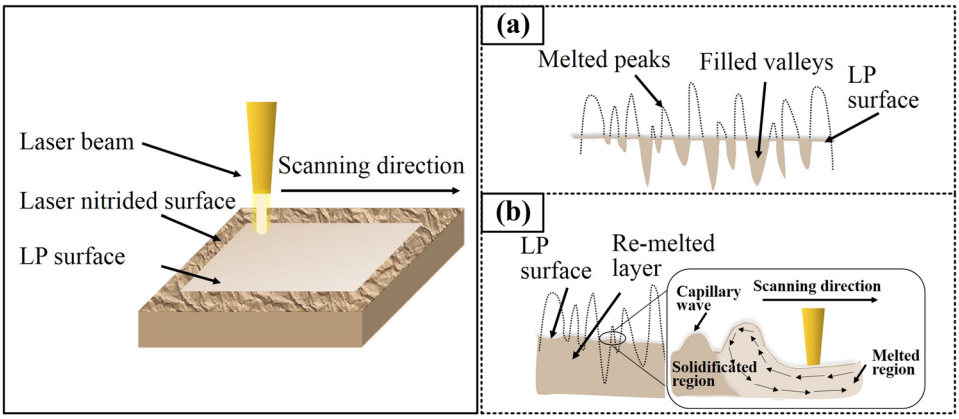

Fig. 2 Schematic diagrams of two typical re-melt related mechanisms in LP: **a** surface shallow melting (SSM) and **b** surface over melting (SOM)

(V), and track overlap (R) based on the preliminary experiments are listed in Table 2.

2.3.2 LP process for surfaces B and C

Since the laser power used in laser nitriding on surfaces B and C was much lower than that used on surface A, the surface roughness of surfaces B and C was much better and relatively lower laser power was needed in the following LP process. Thus, only one LP process was conducted on surfaces B and C and the scanning speed was selected in the range from 100 to 500 mm/s for surfaces B and C. The laser power and track overlap were determined by the pre-experiments, and other parameters used in LP are listed in Tables 3 and 4, respectively.

2.4 Characterization

The surface integrity and morphology of surfaces A, B, and C before and after LP were characterized by laser scanning confocal microscope (LSCM, OLS4100, Olympus, Japan) and tungsten filament scanning electron microscope (SEM, JSM-IT500A, JEOL, Japan), respectively. The areal average roughness (Sa) and areal r.m.s. roughness (Sq) were regarded as the indexes for evaluating the surface integrity. Then, the hardness of the as-cast MG and LP surface was measured by nanoindentation instrument (DUH-211, SHIMADZU, Japan) with a pyramidal indenter (pyramidal indenter, TOKYO DIAMOND Tools MFG. Co., Ltd., Japan).

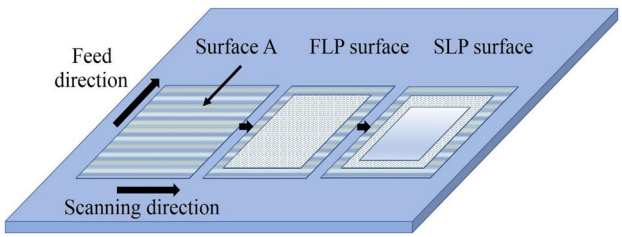

Fig. 3 Schematic diagram of two times of LP on surface A

3 Experimental results and discussion

3.1 Morphologies of laser nitrided surfaces

Figure 4 illustrates the SEM morphologies of the surfaces A, B, and C. In Fig. 4a, remarkable material ablation is occurred on surface A, remaining numerous micro/nanoscale particles along the scanning tracks. While on surface B, due to less laser power, the effect of ablation becomes minor, and small collective laser-induced defects are visible between the adjacent scanning tracks as shown in Fig. 4b. Being different from surfaces A and B, the laser scanning tracks are observed without other noticeable defects on surface C as shown in Fig. 4c. Accompanied with micro-defects in laser nitriding, the surface morphology becomes irregularity and far from its initial surface integrity. Facing this issue, LP was conducted to flatten surfaces A, B, and C for enhancing their surface flatness and roughness.

3.2 Surface roughness after LP on laser nitrided surfaces

3.2.1 Surface roughness after LP on surface A

(A) **Surface roughness after FLP**

Figure 5 illustrates the variation of surface roughness (Sa and Sq) in accordance with the laser power, scanning

Table 2 FLP and SLP parameters on surface A

LP parameter	Value
Laser power (W)	3.75, 5.42, 7.12, 8.82
Scanning speed (mm/s)	100, 200, 300, 400, 500
Track overlap (%)	80, 90

Table 3 LP parameters on surface B

LP parameter	Value
Laser power (W)	3.75, 5.42, 7.12
Scanning speed (mm/s)	100, 200, 300, 400, 500
Track overlap (%)	80

speed, and track overlap after FLP on surface A. From the obtained results in Fig. 5a, it is noted that small laser power (3.75 W) fails to improve the surface roughness. As the laser power increases to 5.42 W, the surface roughness is notably reduced at the scanning speed of 100 mm/s, but the surface flattening effect is gradually decreased with the increase of scanning speed. Further increase of the laser power above 7.12 W leads to a remarkable reduction by approximately 80% in surface roughness regardless of the scanning speed. The above results indicate that surface roughness is remarkably affected by the laser power and scanning speed. According to the Eqs. (1)–(3), the scanning speed affects the laser energy by changing the number of pulses per unit area. Similarly, the relationship between the laser power and laser energy can be described by the following equation:

$$E = P/\left(f \times \pi r^2\right) \tag{4}$$

where E is the energy density, P is the laser power, f stands for the pulse frequency, and r represents the laser spot radius. It is seen that laser power strongly affects the laser energy emitted by the laser beam in case of the fixed pulse frequency and laser spot radius. Therefore, as the laser power or scanning speed changes, the laser energy will change accordingly. Since LP is a thermal energy-based manufacturing process, the laser energy incident on the sample surface majorly contributes to the heat transfer during LP. Therefore, laser energy with different intensities would make the laser irradiated region undergo different melting states (SSM and SOM), thus leading to the variation of the surface roughness.

Next, the effect of the track overlap on surface roughness was investigated. Based on the above experimental results, the laser powers of 7.12 and 8.82 W, which present notable improvement on the surface roughness, were further adopted with different track overlaps, and the corresponding variation of surface roughness is shown in Fig. 5b. It is observed that for each laser power, the track overlap has minor influence on the surface roughness. Nevertheless, the track overlap of 90% would be slightly better in terms of the reduction in surface roughness compared to the track overlap of 80%. In summary, after FLP, the remarkable reduction in surface roughness is obtained at the laser power of 8.82 W, track overlap of 90%, and scanning speeds of 300, 400, and 500 mm/s, as illustrated in Fig. 5b.

Table 4 LP parameters on surface C

LP parameter	Value
Laser power (W)	2.49, 2.78, 3.10, 3.41, 3.75
Scanning speed (mm/s)	100, 200, 300, 400, 500
Track overlap (%)	80

For further evaluating the surface roughness of the FLP surfaces obtained under the above parameters, the 3D morphologies are obtained as shown in Fig. 6. As shown in Fig. 6a–c, the initial surface morphology is removed, but the laser scanning tracks during LP are clearly observed. In addition, some surface defects such as spatial fluctuation and un-melted particles are left on the FLP surface. Thus, the single LP process might be not enough for removing all the surface defects on surface A. To achieve a better surface quality, the second LP should be performed on the surface in Fig. 6b to remove the irregularities and laser scanning tracks.

(B) Surface roughness after SLP

Figure 7 illustrates the variation of surface roughness (Sa and Sq) after SLP in accordance with the laser power and scanning speed. Due to the minor effect of track overlap in FLP, similar performance might be occurred in SLP. Therefore, the track overlap in SLP is kept constant as 80%. As illustrated in Fig. 7, at the laser power of 2.17 or 3.75 W, the surface roughness presents no notable improvement. This may be due to a low laser power (2.17 or 3.75 W) could not provide enough laser energy to melt the surface defects left on the FLP surface. To confirm this speculation, the 3D morphology of the SLP surface under the experimental parameters of $P = 2.17$ W, $V = 400$ mm/s, and $R = 80\%$ is illustrated in Fig. 8a. It is found that the laser scanning tracks and spatial fluctuation are observed, which indicates that the laser power needs to be increased. With the increase of the laser power to 5.42 W, an overall reduction trend in surface roughness is evident. Especially, at the scanning speed of 400 mm/s, the minimum surface roughness of 0.066 μm (Sa) can be achieved. This indicates that the laser energy under this condition is the optimal for surface flattening, and the corresponding 3D morphology is illustrated in Fig. 8b. When the scanning speed is decreased from 400 to 200 mm/s, the distance between the adjacent laser pulses is reduced, leading to the increase of the number of pulses per unit area. Thus, the laser energy excesses the optimal value, leading to a switch of LP mechanism from SSM to SOM. Consequently, the surface materials are over-melted, and capillary waves are generally induced due to the surface tension gradient [33], which limits the reduction in surface roughness, as shown in Fig. 8c. In comparison, as the scanning speed is increased from 400 to 500 mm/s, the current laser energy is insufficient to re-melt the micro-particles

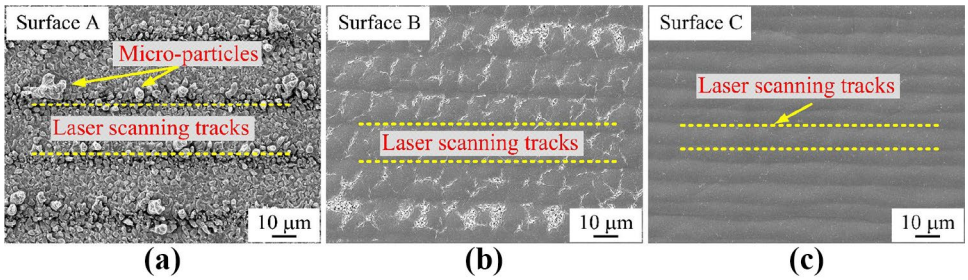

Fig. 4 SEM morphologies of three demonstrated laser nitrided surfaces: **a** surface A, **b** surface B, and **c** surface C

or surface defects, hindering the improvement of surface roughness, as shown in Fig. 8d. According to the above analysis, it can be concluded that by varying the laser power or scanning speed, the absorbed laser energy on the sample surface is different, which leads to the onset of SOM or SSM mechanism, thereby affecting the final surface roughness.

3.2.2 Surface roughness after LP on surface B

Figure 9 illustrates the surface roughness (*Sa* and *Sq*) changing with the laser power and scanning speed, as well as the 3D morphology after LP on surface B. It is observed that as the scanning speed increases from 100 to 500 mm/s, the surface roughness gradually decreases for each laser power. At the scanning speed of 100 mm/s, LP leads to a negative effect on the surface roughness regardless of laser power. For example, when the laser power and scanning speed are 5.42 W and 100 mm/s, the surface roughness of the LP surface is obviously larger than that of surface B as shown in Fig. 9b. As analyzed above, this phenomenon should be related to over-melting of the surface materials caused by excessive laser energy, which can be further confirmed by the capillary waves in Fig. 10a. In addition, the ablation of surface materials is observed in Fig. 10a, which might limit the improvement of surface roughness as well. When the scanning speed increases from 200 to 500 mm/s, surface roughness is gradually decreased for each selected laser power. This may be attributed to the reduction of capillary waves. It is found that when the laser power and scanning speed are 5.42 W and 500 mm/s, the surface roughness (*Sa*) is greatly reduced from 0.059 μm to 0.016 μm, showing a maximum reduction of 72.9%, and smooth LP surface is obtained as shown in Fig. 10b.

3.2.3 Surface roughness after LP on surface C

Figure 11 illustrates the surface roughness (*Sa* and *Sq*) changing with the laser power and scanning speed after LP on surface C as well as the 3D morphology of surface C. Being different from the LP results of surfaces A and B, the roughness of surface C overall tends to increase with the increase of the scanning speed for each laser power. It is observed that when the laser power is set as 3.75 W, the surface roughness is significantly improved. Especially at the LP parameters of $P = 3.75$ W, $V = 300$ mm/s, and $R = 80\%$, the maximum reduction in surface roughness (*Sa*) of 84.6% is obtained, and the flattened LP surface is obtained as shown in Fig. 12a. However, when the scanning speed gradually increases from the 300 mm/s (optimal value) to

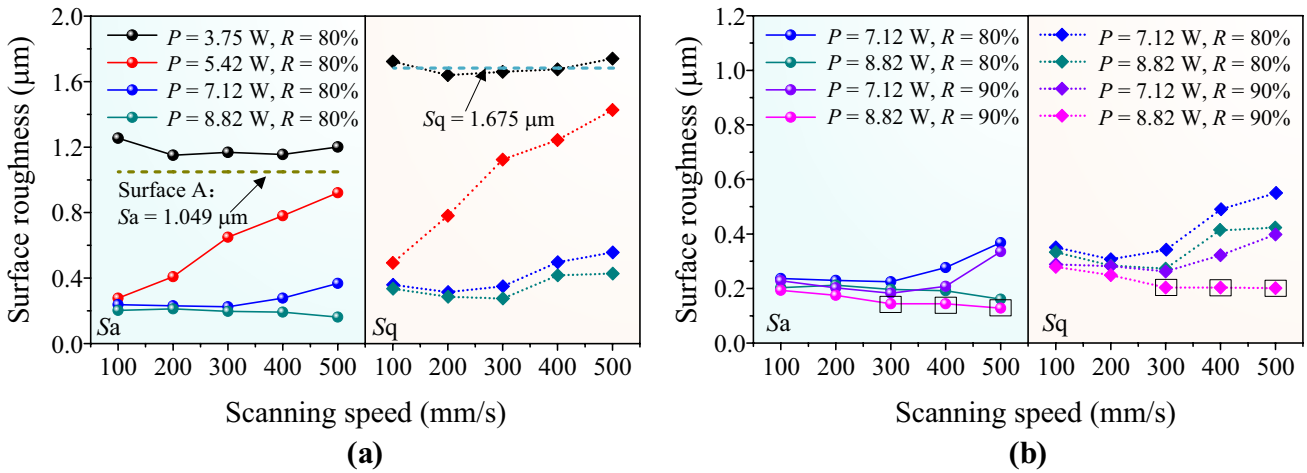

Fig. 5 Surface roughness (*Sa* and *Sq*) after FLP obtained under **a** various laser powers and scanning speeds and **b** various track overlaps

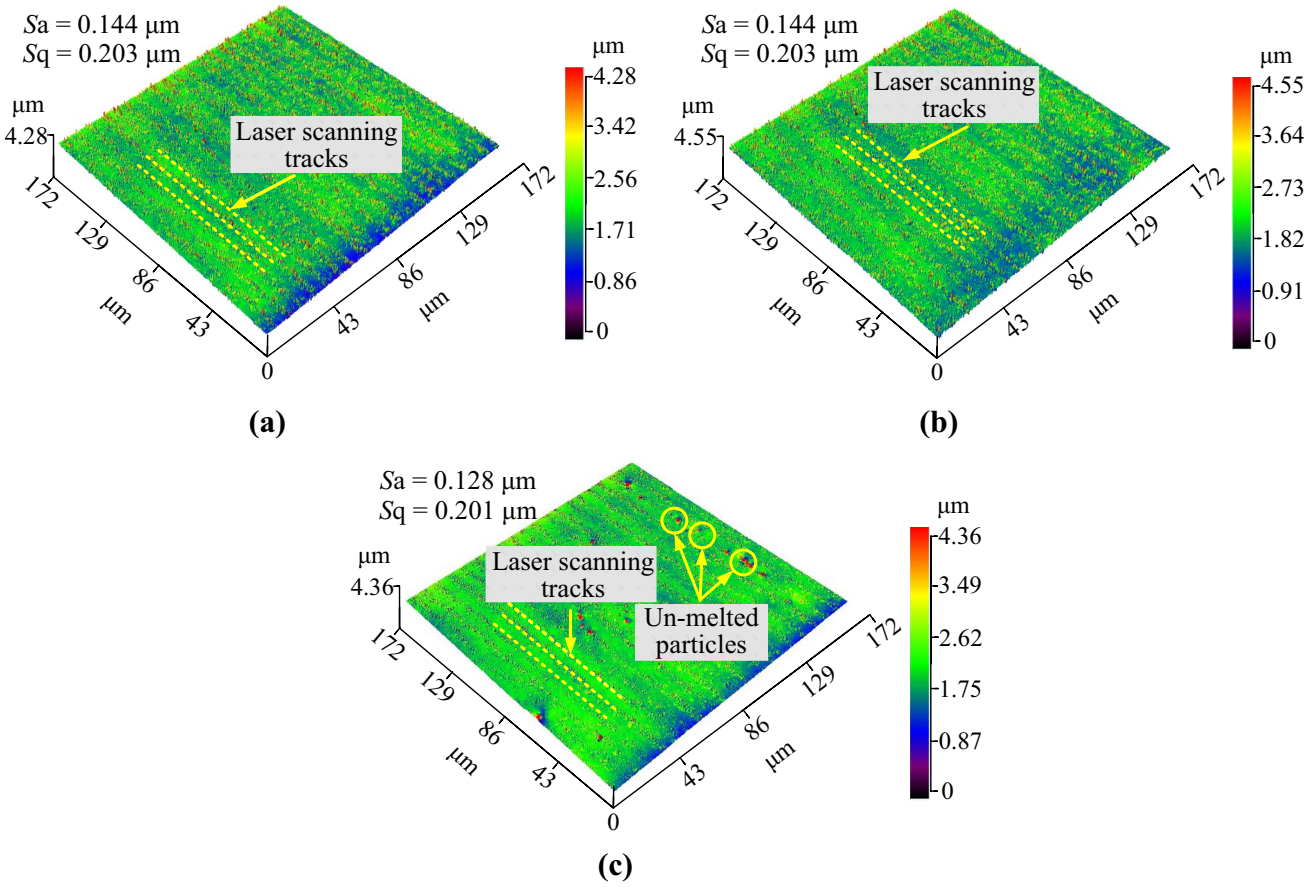

Fig. 6 3D morphologies of surface A after FLP at experimental parameters: **a** $P=8.82$ W, $V=300$ mm/s, and $R=90\%$; **b** $P=8.82$ W, $V=400$ mm/s, and $R=90\%$; and **c** $P=8.82$ W, $V=500$ mm/s, and $R=90\%$

500 mm/s or laser power gradually decreases from 3.75 W to 2.49 W, the surface roughness tends to increase. This may be due to that the valleys on surface C (Fig. 11b) cannot be completely filled caused by the insufficient laser energy. For example, when the laser power and scanning speed are 3.10 W and 500 mm/s, only parts of peaks are melted, thus some residual valleys are still observed on the LP surface as shown in Fig. 12b.

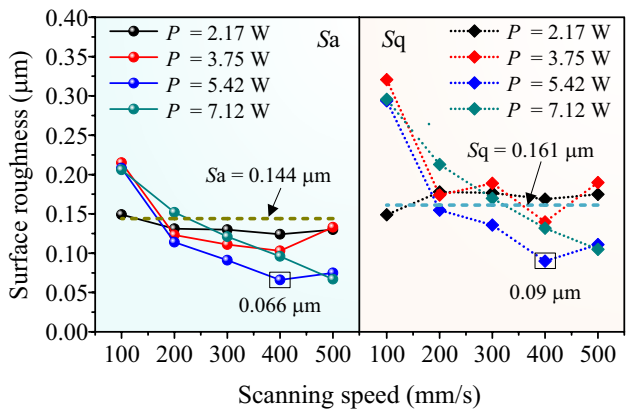

Fig. 7 Surface roughness (*Sa* and *Sq*) after SLP changing with the laser power and scanning speed

3.2.4 LP results on surfaces A, B, and C

From the results of the above experiments, it can be found that the surface roughness for surfaces A, B, and C has been significantly improved by LP, which is mainly attributed to the principle of LP. The corresponding schematic diagram is illustrated in Fig. 13. When the laser beam is focused on the surface of sample, the temperature of the irradiated region rises sharply, resulting in a temperature gradient along the depth direction of sample. Accordingly, the heat is transferred from the surface with high temperature to the interior of sample by convection. Simultaneously, partial heat is dissipated into the environment by radiation, as shown in Fig. 13a. Due to the accumulation of heat, the materials of the irradiated region are melted as shown in Fig. 13b. The degree of melting depends on the laser energy, which is controlled by the laser parameters. When the laser nitrided surface is irradiated with optimal

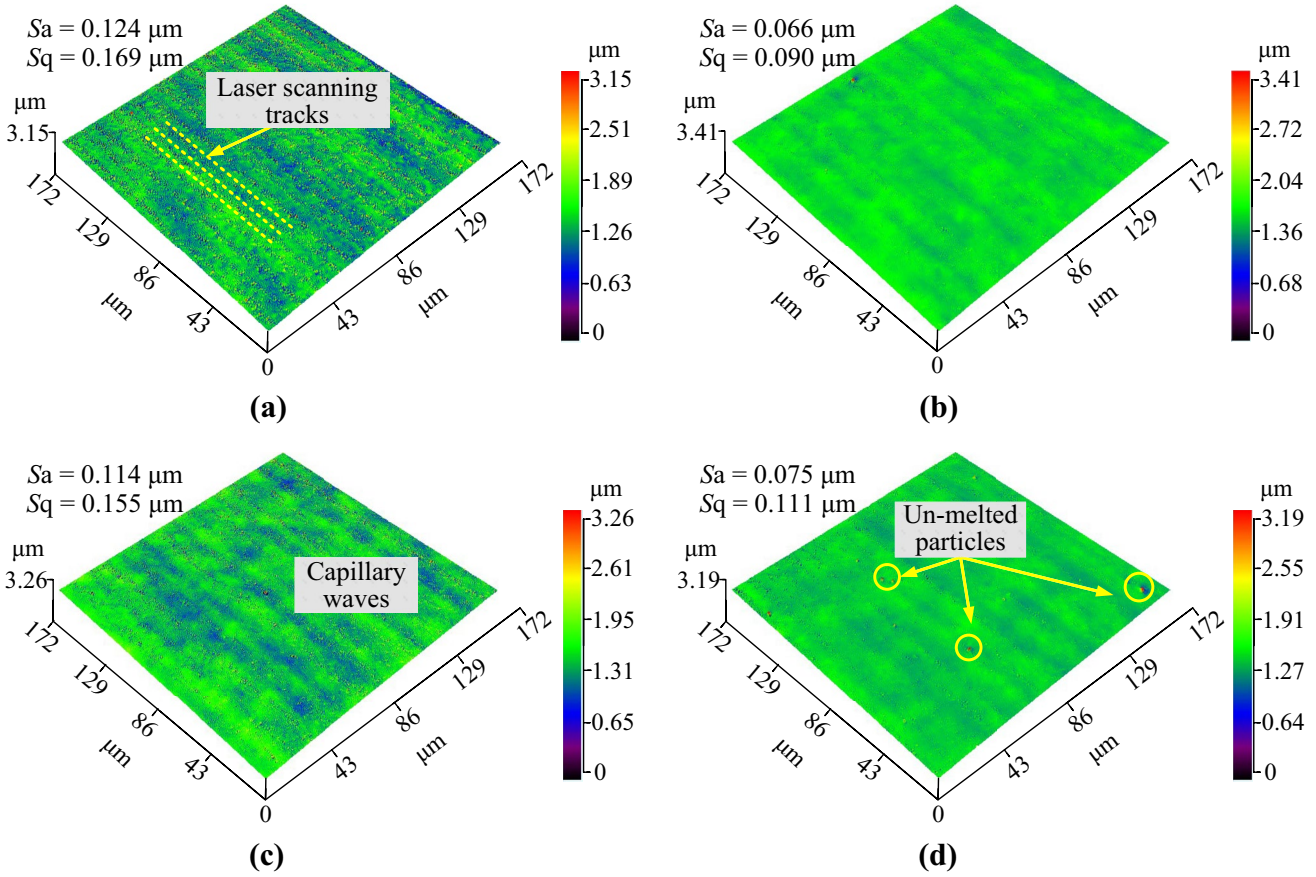

Fig. 8 3D morphologies of the SLP surfaces under the experimental parameters: **a** $P=2.17$ W, $V=400$ mm/s, and $R=80\%$; **b** $P=5.42$ W, $V=400$ mm/s, and $R=80\%$; **c** $P=5.42$ W, $V=200$ mm/s, and $R=80\%$; and **d** $P=5.42$ W, $V=500$ mm/s, and $R=80\%$

laser parameters, its surface defects (spatial fluctuation and particles) are just melted without material ablation, thus leading to the minimum surface roughness. However, when the laser parameters are greater or less than the optimal value, the excessive or insufficient melting occurs, thus hindering the improvement of surface roughness. The

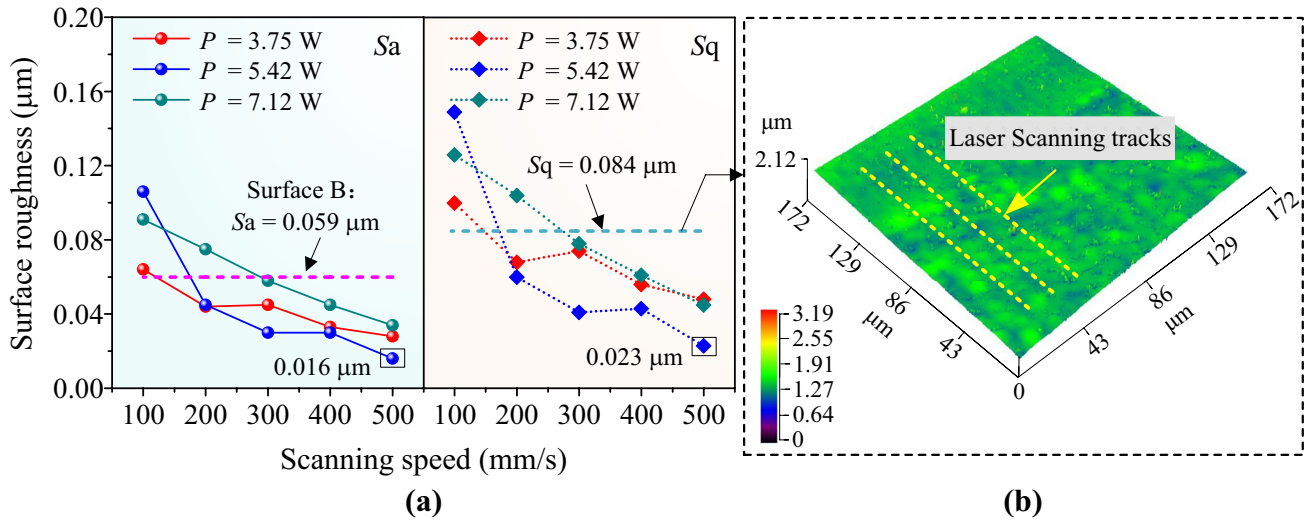

Fig. 9 **a** Surface roughness (*Sa* and *Sq*) changing with laser power and scanning speed after LP on surface B and **b** 3D morphology of surface B

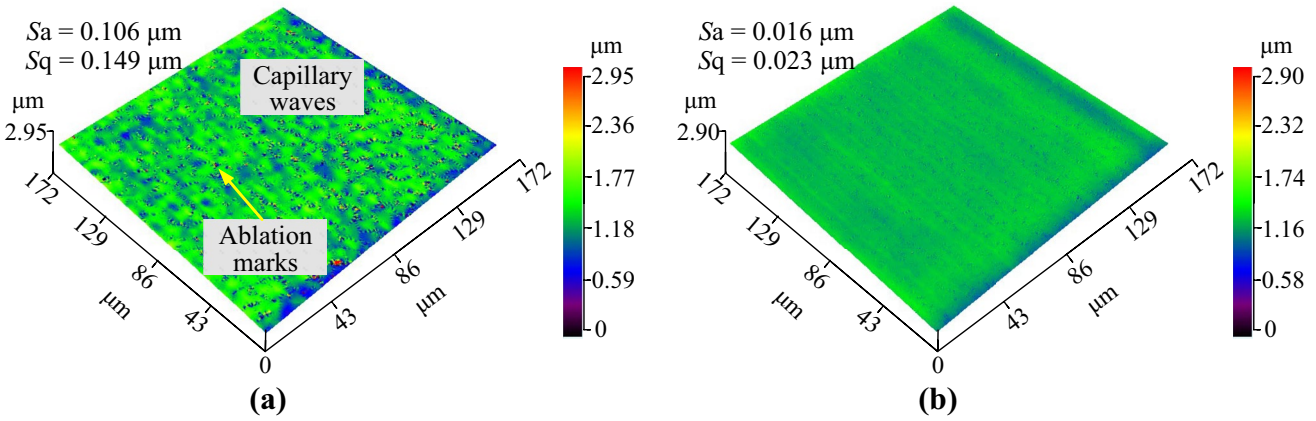

Fig. 10 3D morphologies of the LP surfaces under the experimental parameters: **a** $P = 5.42$ W, $V = 100$ mm/s, and $R = 80\%$; **b** $P = 5.42$ W, $V = 500$ mm/s, and $R = 80\%$

above analysis indicates that appropriate laser parameters play a vital role in improving the surface roughness. For comparing the difference in optimal LP conditions of these three nitrided surfaces and providing reference for similar LP experiments, the roughness of laser nitrided surfaces and LP surfaces, number of LP cycle, laser power, scanning speed, and track overlap are listed in Table 5. It is worth mentioning that the number of LP cycle is greatly affected by the roughness of the initial laser nitrided surface. For flattening surface A, LP is needed to be performed two times (FLP and SLP); while for surfaces B and C, only one LP is needed. In the other word, a rough laser nitrided surface is less likely to achieve remarkable improvement in surface roughness by single LP. Additionally, a relatively high laser power is more suitable for polishing surface with large surface roughness.

3.3 Effect of LP on the microstructure evolution of laser nitrided surface

3.3.1 Effect of LP on the microstructure evolution of surface A

Figure 14 illustrates the micro/nano structures of surface A and the surface morphologies after FLP ($P = 8.82$ W, $V = 400$ mm/s, and $R = 90\%$) and SLP ($P = 5.42$ W, $V = 400$ mm/s, and $R = 80\%$). It is observed that surface A gradually becomes flattened as the number of LP cycle increases, accompanied by the evolution of surface microstructures. As shown in Fig. 14a, b, on surface A, the humps are formed at the overlapped regions of the adjacent laser scanning tracks, accompanied by large numbers of collective micro-particles. The generation of humps may be

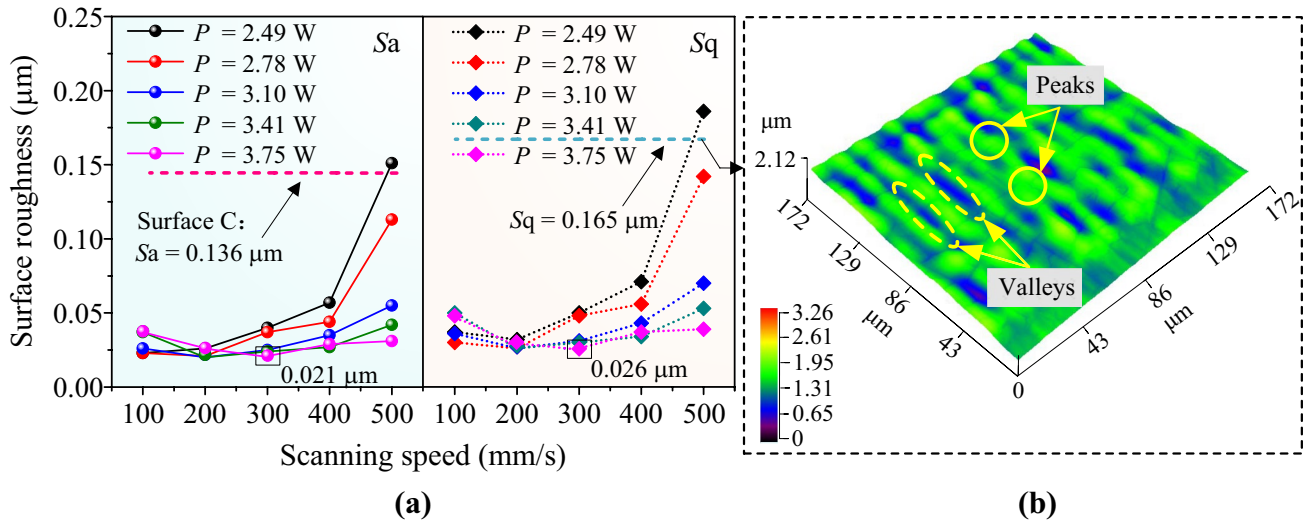

Fig. 11 **a** Surface roughness (*Sa* and *Sq*) changing with the laser power and scanning speed after LP on surface C and **b** 3D morphology of surface C

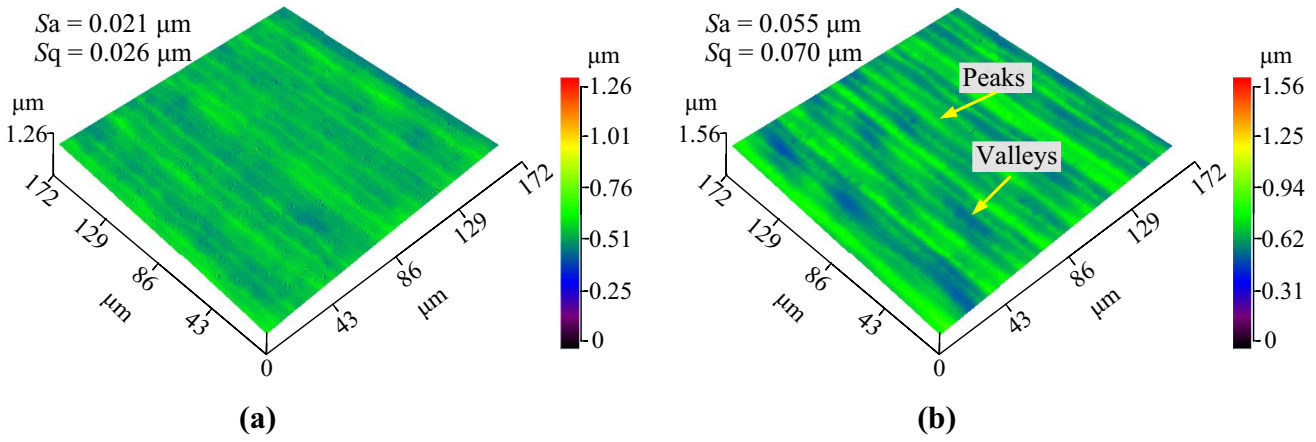

Fig. 12 3D morphologies of the LP surfaces under the experimental parameters: **a** $P = 3.75$ W, $V = 300$ mm/s, and $R = 80\%$; **b** $P = 3.10$ W, $V = 500$ mm/s, and $R = 80\%$

related to the recoil pressure caused by the vaporization of the MG surface materials when irradiated under a high laser energy. Under the action of recoil pressure, the materials of the irradiated region are pushed to flow outward and until they are blocked by the previous laser scanning track, forming the humps [34]. After FLP, surface A is re-melted, thus microparticles disappear and the irregular ripples appear as shown in Fig. 14c, d. The formation of irregular ripples may be attributed to uneven melting caused by inhomogeneities of surface morphology of surface A [35]. In addition, some cracks perpendicular to the scanning tracks are observed on the FLP surface, and these cracks could be caused by the inhomogeneities of solidification rate and thermal stress during LP [36]. After SLP, the surface materials are re-melted again at a small laser energy, and a flat and uniform surface is achieved, as shown in Fig. 14e, f.

3.3.2 Effect of LP on the microstructure evolution of surfaces B and C

Figure 15a, b show the SEM morphologies of surface B and the LP surface, respectively. In Fig. 15a, some irregular stripes caused by material ablation can be observed. These stripes are mainly distributed in the middle of the laser scanning tracks, which should be due to the Gaussian distribution of laser energy [34]. When irradiated by the laser beam, the temperature in the middle of the single laser scanning track is higher than the temperature at the edge, thus the materials in

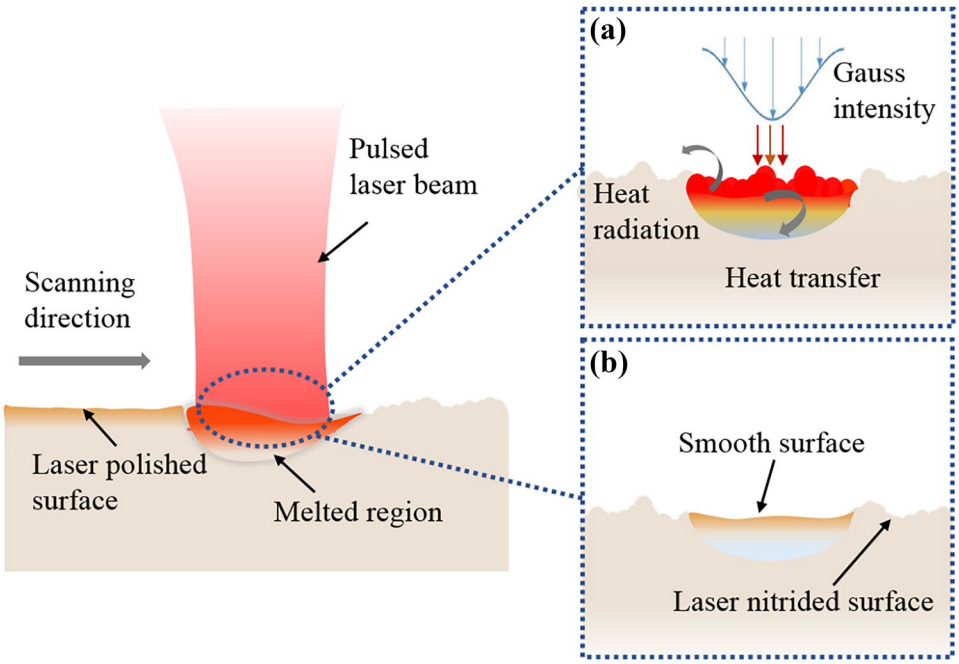

Fig. 13 The schematic diagram of LP on the laser nitrided surface: **a** processes of heat transfer and radiation and **b** smooth surface after LP

Table 5 Optimal LP conditions and results of surfaces A, B, and C

Laser nitrided surface	Surface A	Surface B	Surface C
Roughness of laser nitrided surface (μm)	1.049	0.059	0.136
Roughness of LP surface (μm)	0.066	0.016	0.021
Number of LP cycle	2	1	1
Laser power	8.82/5.42 W	5.42 W	3.75 W
Scanning speed	400/400 mm/s	500 mm/s	300 mm/s
Track overlap	90%/80%	80%	80%

the middle region are easier to be ablated. After LP, the laser scanning tracks and irregular stripes disappear due to the re-melting of surface materials, but some tiny ripples are formed. Nevertheless, surface B becomes flattened after LP. As for surface C, the peaks and valleys generated by multi-line laser scanning can be clearly captured as illustrated in Fig. 15c, and almost no ablation is observed due to the relatively low laser energy. After LP under the optimal parameters, the materials of melted peaks fill up the valleys, which leads to a smooth and homogeneous surface, as shown in Fig. 15d.

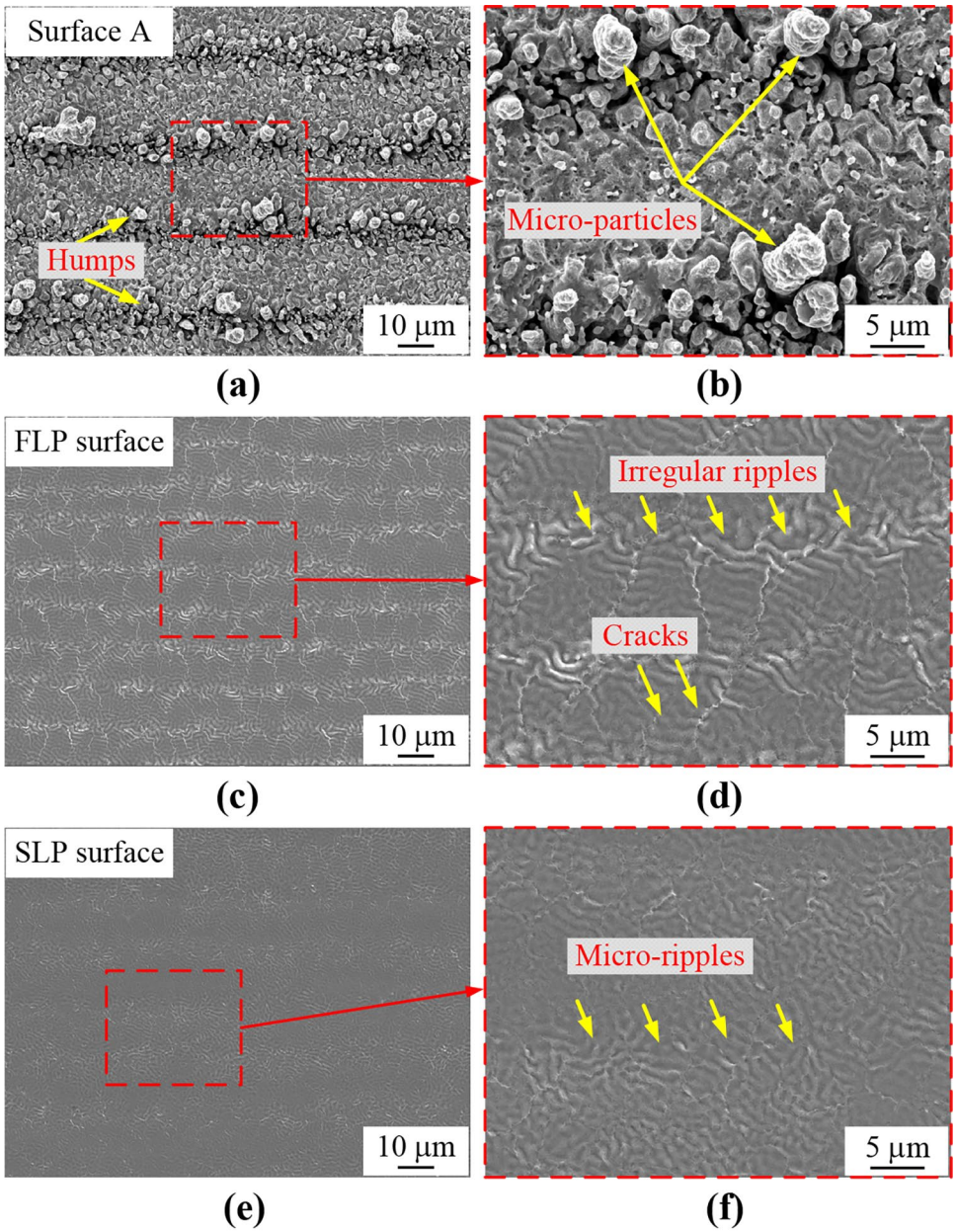

Fig. 14 SEM morphologies of **a** surface A, **c** FLP surface, and **e** SLP surface. The Fig. 14**b**, **d** and **f** are enlarged views of local zones in Fig. 14a, c and e, respectively

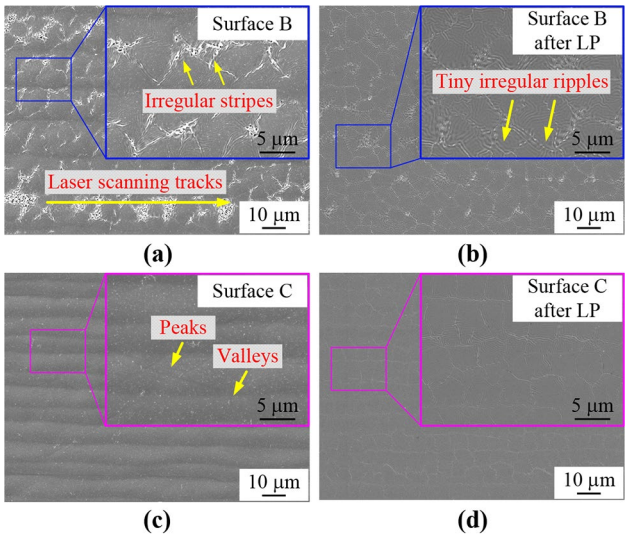

Fig. 15 SEM morphologies of **a** surface B and **c** surface C. The Fig. 15**b**, **d** are morphologies of LP surfaces corresponding to surfaces B and C, respectively

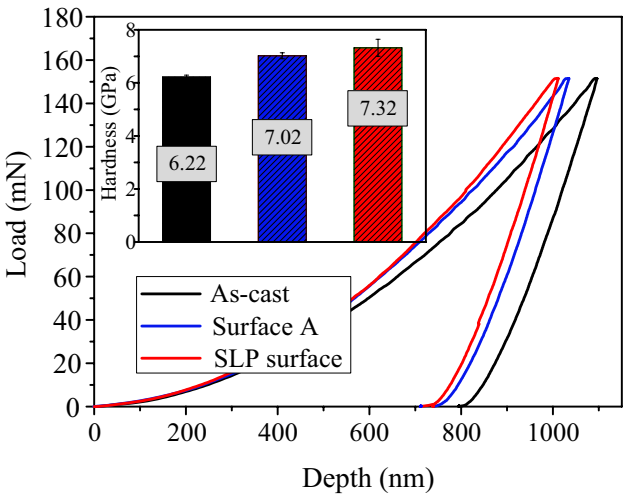

Fig. 16 Load-depth curves and average hardness obtained on the as-cast MG, surface A, and SLP surface under an indentation load of 150 mN

4 Effect of LP on the surface hardness of laser nitrided surface

Besides the enormous improvement in surface roughness of laser nitrided surfaces after LP, the surface hardness of the LP surface was investigated as well. The surface hardness was obtained by nanoindentation tests, and the indentation load and loading rate were 150 mN and 10 mN/s respectively. To eliminate the random error in the tests, nanoindentation tests were repeated ten times at different positions of each surface. Then, the surface hardness of surface A after SLP is given as an example. For comparison, the as-cast MG and surface A are also included. Accordingly, the load-depth curves and average hardness obtained for the as-cast MG, surface A and SLP surface are illustrated in Fig. 16. It is observed that the surface hardness is increased from the as-cast MG of 6.22 GPa to surface A of 7.02 GPa with ~ 12.86% improvement after laser nitriding, and further to SLP surface of 7.32 GPa with ~ 4.27% improvement. It has been reported that the enhancement in surface hardness after laser irradiation in nitrogen atmosphere is related to the introduction of ZrN phase on the surface [19, 37]. Thus, compared to the as-cast MG, the increase in the surface hardness of surface A is caused by ZrN phase. Since LP was also carried out in the nitrogen atmosphere after laser nitriding, therefore, it is reasonable to speculate that the generation and accumulation of ZrN phase during LP lead to the further improvement of the surface hardness of SLP surface. To confirm this, the crystal phases of the as-cast MG, surface A, and SLP surface were characterized by XRD. As illustrated in Fig. 17, the typical amorphous characteristics are exhibited for the as-cast MG, while the peaks of ZrN phase are clearly observed in the patterns for surface A and SLP surface. Furthermore, the intensities of the peaks of ZrN for the SLP surface are slightly stronger, which indicates that the ZrN phase is further accumulated on the surface after SLP. Thus, it can be concluded that the increase in surface hardness of SLP surface is related to the generation of ZrN phase during the laser nitriding and LP processes.

Despite the improvement in surface hardness of the LP surface, further research is conducted to explore whether much higher surface hardness could be obtained by laser nitriding and the subsequent LP. As analyzed above, laser nitriding has a greater impact on improving the surface hardness than LP. Therefore, in order to further improve the surface hardness of the LP surface, the parameters for the initial

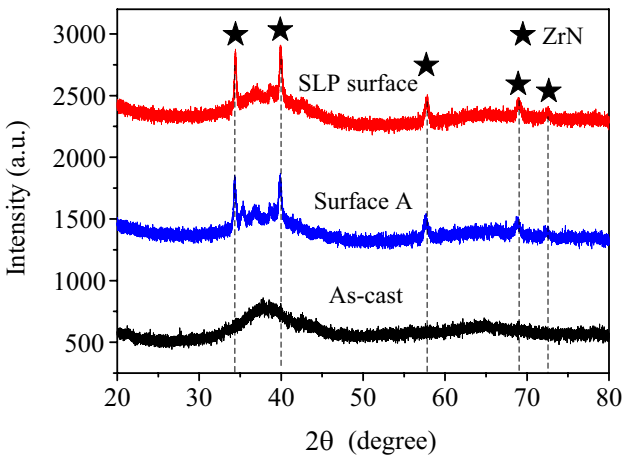

Fig. 17 XRD patterns obtained for the as-cast MG, surface A, and SLP surface

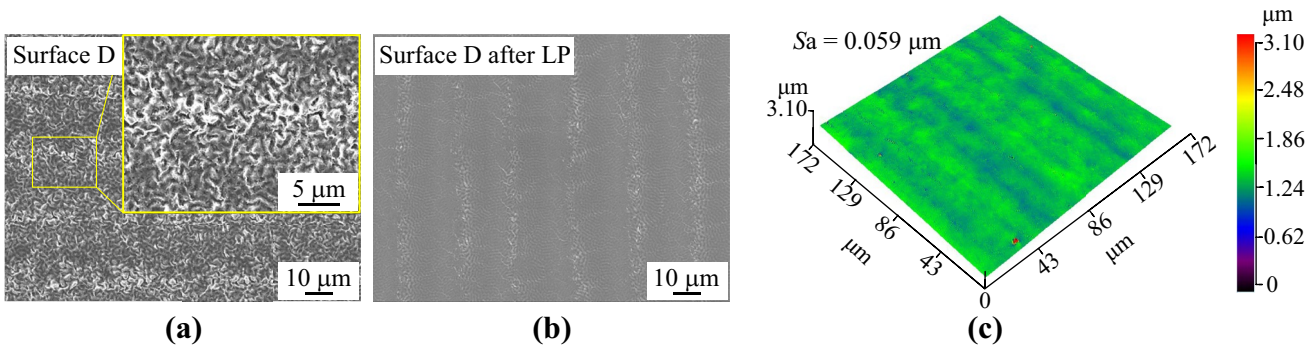

Fig. 18 SEM morphologies of **a** surface D, **b** surface D after LP, and **c** 3D morphologies after LP

laser nitriding process are critical. In the following experiment, another set of laser nitriding parameters is selected based on the above experiments for supporting the inference.

Accordingly, another laser nitrided surface (surface D) was prepared under the laser nitriding parameters of $P = 5.42$ W, $V = 20$ mm/s, and $R = 50\%$, which employed higher laser power in laser nitriding. The SEM morphology is shown in Fig. 18a. It is observed that surface D is covered by tinny ripples without obvious peaks and valleys. After LP at the optimal LP parameters ($P = 10.5$ W, $V = 400$ mm/s, and $R = 80\%$), the surface roughness of surface D is greatly reduced from 0.106 μm to 0.054 μm. The SEM morphology and 3D morphologies of the LP surfaces are shown in Fig. 18b, c, respectively. Accordingly, the same nanoindentation tests were performed on the LP surface, and the corresponding surface hardness and residual indent morphologies are illustrated in Fig. 19. From the obtained results, the surface hardness is greatly increased to 8.03 GPa after laser nitriding (~29.1% enhancement), and further increased to 8.31 GPa after LP (~3.5% enhancement). It is clearly observed that even though the surface hardness of the LP surface is further increased, the laser nitriding plays a vital role in the increase of surface hardness.

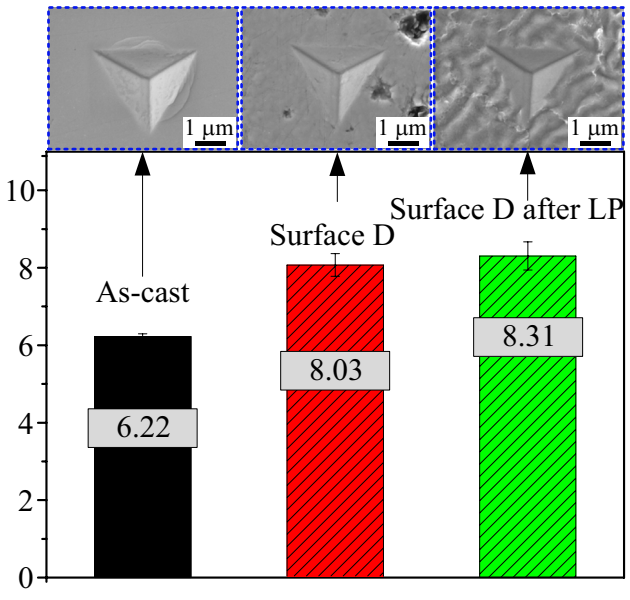

Fig. 19 Surface hardness and residual indent morphologies observed for the as-cast MG surface, surface D, and surface D after LP. The nanoindentation parameters are the same with the above experiment

5 Conclusions

In the paper, LP was performed to flatten the laser nitrided Zr-based MG surfaces, and its feasibility was demonstrated through polishing three types of laser nitrided surfaces with different initial morphologies (surfaces A, B, and C). By systematic experiments and analysis, the following conclusions could be obtained:

1. For surface A, LP process is performed consecutively two times (FLP and SLP), and the surface roughness (*S*a) is greatly decreased from 1.049 μm to 0.144 μm by FLP, and further decreased to 0.066 μm by SLP, achieving a remarkable reduction in surface roughness (*S*a) of 93.7%. While for surfaces B and C, the maximum reductions in surface roughness (*S*a) after only single LP are 72.9% (from 0.059 μm to 0.016 μm) and 84.6% (from 0.136 μm to 0.021 μm), respectively. In addition, due to the re-melting of the surface materials caused by LP, most of the surface defects such as lumps, cracks, and microparticles have been fully removed. It is indicated that LP is an effective method to improve the surface quality.
2. By varying the scanning speed or laser power, the laser energy on the sample surface is different, leading to the different mechanisms of LP, involving SOM or SSM, which in turn dominates the final surface roughness.
3. The increase in surface hardness of the LP surface has been observed compared to the as-cast MG surface, which should be attributed to the generation and accumulation of ZrN phase in laser nitriding and the following LP.

Author contribution HH: supervision, resources, conceptualization, investigation, methodology, and data curation; JH: visualization, analysis, and writing—original draft; YQ: methodology, validation, and writing—review; CW: validation and writing—review; ZZ: methodology, resources, and validation; LZ: validation, data curation, and writing—review and editing.

Funding This work was supported by the National Natural Science Foundation of China (grant no. 51705197), Science and Technology Project from the Education Department of Jilin Province (grant no. JJKH20190014KJ), and Young Elite Scientists Sponsorship Program by CAST(YESS) (grant no. 2017QNRC001), and the Fundamental Research Funds for the Central Universities (2020–2022).

Availability of data and material The data sets generated and analyzed from the current study are available upon request from the corresponding author.

Code availability Not applicable.

Declarations

Ethics approval Not applicable.

Consent to participate Not applicable.

Consent for publication Not applicable.

Conflict of interest The authors declare no competing interests.

References

1. Jun WK, Willens RH, Duwez P (1960) Non-crystalline structure in solidified gold–silicon alloys. Nature 187:869–870
2. Inoue A, Kita K, Zhang T, Masumoto T (1989) An amorphous La55Al25Ni20 alloy prepared by water quenching. Mater Trans 30:722–725
3. Ashby MF, Greer AL (2006) Metallic glasses as structural materials. Scripta Mater 54:321–326
4. Schroers J (2010) Processing of bulk metallic glass. Adv Mater 22:1566–1597
5. Lu J, Ravichandran G, Johnson WL (2003) Deformation behavior of the Zr41.2Ti13.8CU12.5Ni10Be22.5 bulk metallic glass over a wide range of strain-rates and temperatures. Acta Mater 51:3429–3443
6. Wang WH, Li FY, Pan MX, Zhao DQ, Wang RJ (2004) Elastic property and its response to pressure in a typical bulk metallic glass. Acta Mater 52:715–719
7. Wang WH, Li LL, Pan MX, Wang RJ (2001) Characteristics of the glass transition and supercooled liquid state of the Zr41Ti14Cu12.5Ni10Be22.5 bulk metallic glass. Phys Rev B 63:52204–52204
8. Greer AL (1995) Metallic glasses. Science 267:1947–1953
9. Inoue A (2000) Stabilization of metallic supercooled liquid and bulk amorphous alloys. Acta Mater 48:279–306
10. Jiang MQ, Dai LH (2009) On the origin of shear banding instability in metallic glasses. J Mech Phys Solids 57:1267–1292
11. Lewandowski JJ, Greer AL (2006) Temperature rise at shear bands in metallic glasses. Nat Mater 5:15–18
12. Man HC, Cui ZD, Yang XJ (2002) Analysis of laser gas nitrided titanium by X-ray photoelectron spectroscopy. Appl Surf Sci 199:293–302
13. Kathuria YP (2007) Laser surface nitriding of yttria stabilized tetragonal zirconia. Surf Coat Technol 201:5865–5869
14. Fu J, Zhu YH, Zheng C, Liu R, Ji Z (2016) Effect of laser shock peening on the compressive deformation and plastic behavior of Zr-based bulk metallic glass. Opt Laser Eng 86:53–61
15. Chan CW, Lee S, Smith GC, Donaghy C (2017) Fibre laser nitriding of titanium and its alloy in open atmosphere for orthopaedic implant applications: investigations on surface quality, microstructure and tribological properties. Surf Coat Technol 309:628–640
16. Obeidi MA, McCarthy E, Brabazon D (2018) Laser surface processing with controlled nitrogen-argon concentration levels for regulated surface life time. Opt Laser Eng 102:154–160
17. Donaghy CL, McFadden R, Kelaini S, Carson L, Margariti A, Chan CW (2020) Creating an antibacterial surface on beta TNZT alloys for hip implant applications by laser nitriding. Opt Laser Technol 121:105793
18. Li YS, Zhang K, Wang Y, Tang WQ, Zhang YT, Wei BC, Hu Z (2020) Abnormal softening of Ti-metallic glasses during nanosecond laser shock peening. Mat Sci Eng A 773:138844
19. Huang H, Jiang MQ, Yan JW (2018) The coupling effects of laser thermal shock and surface nitridation on mechanical properties of Zr-based metallic glass. J Alloy Compd 770:864–874
20. Zhang BC, Li XH, Bai JM, Guo JF, Wang P, Sun CN, Nai ML, Qi GJ, Wei J (2017) Study of selective laser melting (SLM) Inconel 718 part surface improvement by electrochemical polishing. Mater Design 116:531–537
21. Dong Y, Lei H, Liu WQ, Wang TX, Xu L (2018) Preparation of non-spherical silica composite abrasives by lanthanum ion-induced effect and its chemical-mechanical polishing properties on sapphire substrates. J Mater Sci 53:10732–10742
22. Lamikiz A, Sánchez J, Lacalle L, Arana JL (2007) Laser polishing of parts built up by selective laser sintering. Int J Mach Tool Manu 47:2040–2050
23. Ma CP, Guan YC, Zhou W (2017) Laser polishing of additive manufactured Ti alloys. Opt Laser Eng 93:171–177
24. Weingarten C, Schmickler A, Willenborg E, Wissenbach K, Poprawe R (2017) Laser polishing and laser shape correction of optical glass. J Laser Appl 29:011702
25. Lambiase F, Genna S, Leone C (2020) Laser finishing of 3D printed parts produced by material extrusion. Opt Laser Eng 124:105801
26. Tseng SF, Chen YS (2021) Surface microtexturing of Ti-6Al-4V and SS316L alloys using high pulsed fiber lasers for improving the adhesive bonded performance. Opt Laser Technol 143:107349
27. Tseng SF, Liao CH, Hsiao WT, Chang TL (2021) Ultrafast laser direct writing of screen-printed graphene-based strain electrodes for sensing glass deformation. Ceram Int 47:29099–29108
28. Tseng SF, Liao CH (2020) Investigation of interactions between ultrafast laser beams and screen-printed silver nanopaste films. Appl Surf Sci 512:144696
29. Tseng SF, Huang CC (2021) Investigation of interactions between high pulsed ultraviolet lasers and composite graphene/AgNWs films. Appl Surf Sci 570:151060
30. Bordatchev EV, Hafiz AMK, Tutunea-Fatan OR (2014) Performance of laser polishing in finishing of metallic surfaces. Int J Adv Manuf Technol 73:35–52
31. Ramos JA, Bourell DL, Beaman JJ (2002) Surface over-melt during laser polishing of indirect-SLS metal parts. MRS Proc 758(LL1):9
32. Krishnan A, Fang F (2019) Review on mechanism and process of surface polishing using lasers. Front Mech Eng-prc 14:299–319
33. Yung KC, Zhang SS, Duan L, Choy HS, Cai ZX (2019) Laser polishing of additive manufactured tool steel components using

pulsed or continuous-wave lasers. Int J Adv Manuf Technol 105:425–440
34. Huang H, Yan JW (2017) Surface patterning of Zr-based metallic glass by laser irradiation induced selective thermoplastic extrusion in nitrogen gas. J Micromech Microeng 27:075007
35. Nusser C, Kumstel J, Kiedrowski T, Diatlov A, Willenborg E (2015) Process- and material-induced surface structures during laser polishing. Adv Eng Mater 17:268–277
36. Xu Z, Ouyang W, Liu Y, Jiao J, Zhang W (2021) Effects of laser polishing on surface morphology and mechanical properties of additive manufactured TiAl components. J Manuf Process 65:51–59
37. Reger NC, Balla VK, Da SM, Bhargava AK (2017) Wear and corrosion properties of in-situ grown zirconium nitride layers for implant applications. Surf Coat Technol 334:357–364